Energy & Environmental Science

Demonstration of 10+ Hour Energy Storage with Φ1" Laboratory Size Solid Oxide Iron-Air Battery

Journal:	*Energy & Environmental Science*
Manuscript ID	EE-ART-05-2022-001626.R2
Article Type:	Paper
Date Submitted by the Author:	23-Aug-2022
Complete List of Authors:	Tang, Qiming ; University of South Carolina, Mechanical Engineering; University of South Carolina Zhang, Yongliang; University of South Carolina System, Mechanical Engineering Xu, Nansheng; University of South Carolina System, Mechanical Engineering Lei, Xueling; Jiangxi Normal University, Huang, Kevin; University of South Carolina System, Mechanical Engineering

Demonstration of 10+ Hour Energy Storage with ϕ1″ Laboratory Size Solid Oxide Iron-Air Battery

Qiming Tang[1], Yongliang Zhang[1], Nansheng Xu[1], Xueling Lei[2] and Kevin Huang[1]**

[1]Department of Mechanical Engineering, University of South Carolina, Columbia, SC 29201, USA

[2] Department of Physics, Jiangxi Normal University, Nanchang, Jiangxi 330022, China

*Corresponding author: huang46@cec.sc.edu; xueling@mail.ustc.edu.cn

Abstract

Long duration electricity storage (LDES) with 10+ hour cycle duration is an economically competitive strategy to accelerate the penetration of renewable energy into the utility market. Unfortunately, none of the available energy storage technologies can meet the LDES' requirements for duration and cost. The newly emerged solid-oxide iron-air batteries (SOIABs) with energy-dense solid iron as the energy storage material have inherent advantages for LDES applications. Here we report for the first time the LDES capability of SOIAB even at a laboratory scale. We show that SOIAB with an Ir-catalyzed Fe-bed can achieve excellent energy density (625 Wh/kg), long cycle duration (12.5 h) and high round-trip efficiency (~90%) under LDES-related working conditions. Given the excellent low-rate performance and the use of earth-abundant, low-cost Fe as the energy storage material, we conclude that SOIAB is a well-suited battery technology for LDES applications.

Keywords: oxide-ion chemistry, Fe-based storage materials, Fe-utilization, round-trip efficiency, catalyst.

1. Introduction

Cost-effective, large-scale stationary electricity storage systems play a critical role in achieving resilient grid stability and accelerating renewable energy penetration into the utility market. Recent analyses suggest that long-duration electricity storage (LDES) with multi-day storage and even seasonal energy arbitrage will have significant advantages in promoting deeper penetration of low-cost wind and solar powers [1-6]. As of today, most commercial electricity storage deployments, as well as research & development, focus primarily on systems with durations ≤ 10 hours at rated power [7, 8]. For example, today's most dominant large-scale electricity storage technologies (*e.g.,* pumped-hydro storage (PHS)) can only store up to 10 hours energy, which only satisfies applications of daily baseload energy time-shift and cannot leverage the full benefits of LDES. Conventional Li-ion batteries are also severely limited in extending storage durations beyond 10 hours due to the high costs to scale up, not to mention the safety concern on using clustered Li-ion battery systems. Redox flow batteries are scalable and safe, but their low energy density and efficiency have also constrained their applications in LDES. Therefore, there is a significant lack of viable LDES technologies on the utility market.

To address this technological gap, the author's group has recently developed a new type of all solid-state battery operated on oxide-ion chemistry, *viz.* solid-oxide iron-air battery (SOIAB), in which the chemical energy of oxygen as transported in the form of O^{2-} is reversibly stored in an energy-dense Fe/FeO_x-bed (or abbreviated as "Fe-bed" throughout this paper) that is integrated within the anode chamber of a reversible solid oxide cell (RSOC) [9-12]. **Figure 1** schematically shows the SOIAB consisting of an RSOC and Fe-bed or the Energy Storage Unit

(ESU). In this battery design, the oxygen electrode (OE) and hydrogen electrode (HE) are open to air of an unlimited oxygen source and enclosed to a low-cost Fe-bed chamber, respectively. During cycling, RSOC alternately operates in fuel cell mode during discharge and electrolyzer mode during charge, while the oxygen is being transferred via a gas-phase H_2/H_2O shuttle and stored within the Fe-bed via the Fe-O redox reaction. One unique feature of SOIAB is its free access to oxygen in air (thus no oxygen storage needed for OE), making it easy for LDES applications [9].

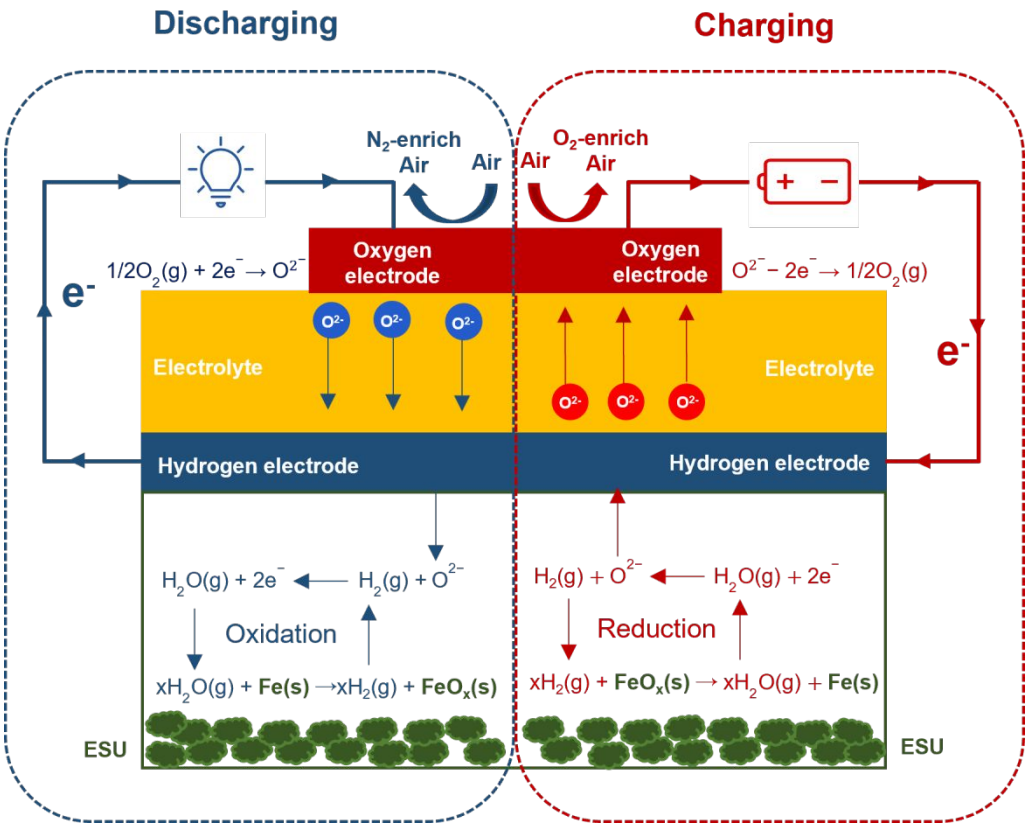

Figure 1. Schematic of the working principle of the all-solid oxide Fe-air battery.

Realizing the durability and cost issues for conventional high-temperature (700-800°C) RSOCs, our early research effort on SOIAB has been mainly focused on developing key enabling materials for intermediate temperature (IT) 500-600°C operation. During the development, we realize that while the durability of IT-SOIAB can be significantly improved at IT, its rate

performance is limited by the higher electrode overpotentials and more sluggish FeO_x reduction kinetics. For example, a 550°C-SOIAB can cycle at a low rate (*e.g.* 0.2 C or 10 mA/cm^2 for a 1.4 cm^2 cell) and low Fe-utilization (U_{Fe}=3.1% of 0.01 mole Fe loading) for 150 hours (or 500 cycles) without any noticeable degradation, but it degrades much faster at higher C-rates and U_{Fe} [9, 13]. SOIAB's low rate-performance, while not suitable for applications requiring fast charge and discharge cycles, might not necessarily be a problem for LDES if there is enough Fe available in the battery to store energy (electricity equivalent to O^{2-}). For example, a simple calculation based on Faraday's law indicates that 67.3 kg of Fe is needed to store electricity for 24 hours at a current of 100 A and Fe-utilization (U_{Fe}) of 20% (see Figure S1a and S1b in the Supporting Information, SI). Since Fe-mass exclusively determines the energy capacity of an SOIAB, we will use Fe-mass in the Fe-bed to express the specific energy densities achieved under different conditions for comparison purpose in this work. It should also be a good estimate of the energy storage capacity that a practical SOIAB system can offer since LDES applications are stationary and the total weight of the system plays a minor role.

It is also interesting to note that energy (size of Fe-bed) and power (area of electrode) can be separately pursued in SOIAB systems for user-specific applications. We can envision that a large Fe-bed can sustain electricity storage for months or even the entire renewable-rich season under a low power mode. We also acknowledge that the charging process (electrolysis) is endothermic, which could influence the temperature uniformity across the battery. However, like any high temperature solid oxide electrolytic cells, by operating the cell voltage at near thermoneutral potential can mitigate the need for extra heat to keep the temperature stable. For SOIAB, this thermoneutral potential is 1.40 V at 550°C, which falls well within the operating

voltage range. Therefore, in addition to many other advantages of Fe-bed materials (*e.g.*, earth abundance and low cost), it is reasonable to deem IT-SOIAB a potential technology for LDES.

From our early work, we have identified two major problems limiting the overall performance of a SOIAB: 1) Fe-bed's sluggish FeO_x-to-Fe reduction kinetics; [14] 2) RSOC's high electrode overpotentials.[9] To address these issues, we have previously shown that synthesis of nanostructured Fe-bed materials [11] and addition of catalyst (*e.g.*, Pd) nanoparticles can boost the FeO_x-to-Fe reduction kinetics.[9] However, our effort to further improve RSOC's electrochemical performance has been very limited in the past.

Here we report our recent effort in improving the performance of the components in an SOIAB. We first show how OE, electrolyte thickness, and HE impact the RSOC's performance by using a three-electrode symmetrical cell combined with DC-biased electrochemical impedance spectroscopy (EIS) methodology. The obtained overpotential (η) vs. current density (j) relationship of OE under both fuel cell and electrolyzer modes is then combined with the V-j curve of a full battery cell to separate the individual contribution from OE, electrolyte, and HE. We then show how the performance (specific energy density, round-trip efficiency (RTE) and cycle life) of SOIAB is affected by C-rate and U_{Fe}. We also show how Ir catalyst in the Fe-based ESU boosts the charging (FeO_x reduction) performance of SOIAB at both low and high U_{Fe}. Finally, by combining improved RSOC with Ir-catalyzed Fe-bed, we demonstrate the LDES performance with multiple stable 12.5-hour charge/discharge cycles on an $\phi 1''$ size SOIAB.

2. Results and Discussion

2.1. Cell microstructure and composition

A detailed description on the fabrication process is provide in the Experimental Procedure section. The cross-sectional view of microstructure of the baseline HE-supported cell fabricated by dip-coating method is shown in Figure 2a, where a 10-μm thick, dense ScSZ electrolyte and 10-μm thick, porous HE functional layer are clearly seen deposited on the HE-support (~400 μm thick). Figure 2b shows the microstructure of HE-support with a pore size in the range of 3-5 μm after reduction in H_2-3% H_2O at 550 ^oC. For the best performing RSOC with 2 wt.% gadolinium-doped ceria (GDC) infiltrated HE-support (to be shown later), Figure 2c shows a similar after-reduction microstructure to Figure 2b, but the infiltrated GDC appears to be present as a thin layer on the Ni-ScSZ surface (see the insert in Figure 2c). The microstructures of OE/electrolyte interface before and testing for 250 hours under 0.2C and 550^{o}C are shown in Figure S2. No significant change was found.

To further examine the morphology of GDC infiltrant, we performed STEM on the GDC layer. While there is no GDC present in the baseline HE, see Figure 2d, Figure 2e shows a roughly 20 nm thick GDC layer on the surface of ScSZ/NiO particles for the 2 wt.% GDC sample, while it is thicker (~40-80 nm) for the 4 wt.% GDC sample, see Figure 2f and Figure S3-S5. The HE with 2 wt.% GDC was further analyzed after testing for 500 hours. Figure 2g shows the STEM image of an ScSZ particle coated with a ~20 nm thick GDC and Ni layer. Both GDC with Ni phases play an active catalytic role in promoting H_2 oxidation and H_2O reduction reactions during cycling. The elemental mapping in Figure 2g1-2g6 provides an expected uniform distribution of Zr, Sc, O, Ni, Ce and Gd around an ScSZ particle; their semiquantitative

contents analyzed by SEM-EDS are given in Figure S6, which further confirms the STEM-EDS results.

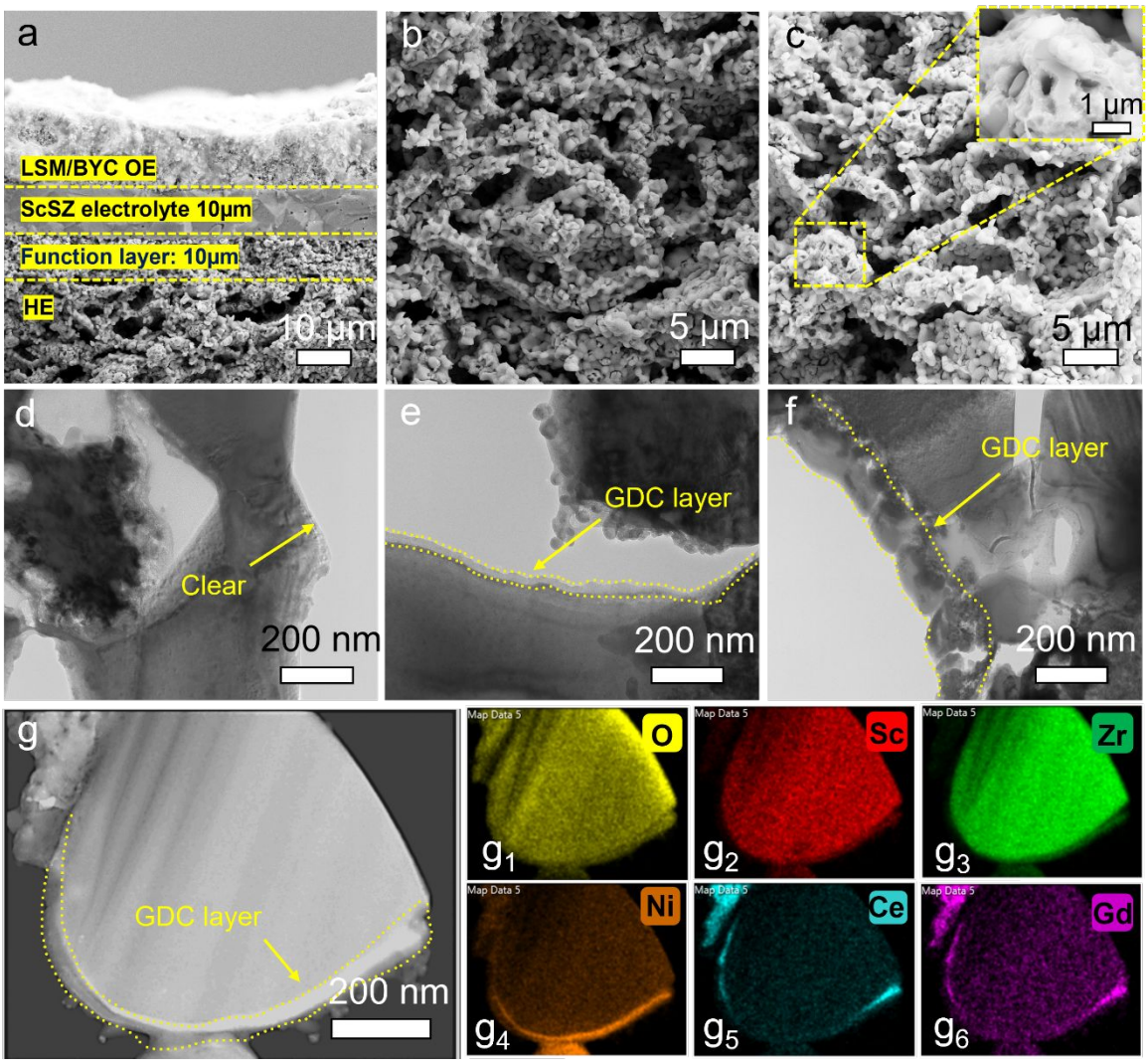

Figure 2. (a) Cross-sectional SEM micrographs of the fabricated pre-reduction HE-supported cell by dip-coating; (b) HE microstructure after H_2-reduction; (c) 2 wt.% GDC infiltrated HE microstructure; (d) TEM images of the baseline HE-supported cell; (e) HE-support with 2 wt.% GDC; (f) HE-support with 4 wt.% GDC; (g) STEM mapping of a HE particle with 2 wt.% GDC after testing.

2.2. Fe-bed morphology and composition

The chemical compositions of the Fe-bed material, *i.e.* Fe_2O_3/ZrO_2 (the use of ZrO_2 is to mitigate Fe particle sintering) and IrO_2 impregnated Fe_2O_3/ZrO_2 composite were determined by XRD; the results are shown in Figure S7. The pristine Fe_2O_3/ZrO_2 powders show peaks at

2θ= 24, 33.2, 25.6, 40.8, 49.5 and 54.1 °, which are assigned to (012), (104), (110), (113), (024) and (116) planes of Fe_2O_3 (PDF # 33-0664). The peaks at 2θ=28.1 ° and 35.1 ° can be indexed to $(\bar{1}11)$ and (002) planes of ZrO_2, respectively. The sharp peaks free of any other impurity phase suggest a high crystallinity and purity of the sample. After introducing IrO_2, no new peaks can be observed. However, its intensity and shape of the peak appear to be weaker and broader, implying relatively low crystallinity of IrO_2 particles in the sample. In addition, metallic Fe and ZrO_2 are found in the cycled Fe_3O_4/ZrO_2-Ir sample, suggesting that the iron oxide has been fully reduced to iron.

The morphology of the pristine Fe_2O_3/ZrO_2 powder is shown in SEM images of Figure 3a; a slight agglomeration is observed, which is not surprising given the thermal treatment of the powder after the synthesis. After adding IrO_2, Figure 3b shows Fe_2O_3/ZrO_2 particles are covered with discrete IrO_2 nanoparticles (NPs) in a size of ~5 nm (see Figure 3c and Figure S8). In addition, the high-resolution TEM (HRTEM) image of Figure 3c indicates crystalline fringes matching well to Fe_2O_3, ZrO_2 and IrO_2, *i.e.,* 0.51, 0.31, 0.36, 0.27 and 0.23 nm corresponding to (100) and $(\bar{1}11)$ planes of ZrO_2, (110) and (104) planes of Fe_2O_3, and (200) plane of IrO_2, respectively. The IrO_2 NPs uniformly distributed on the surface of Fe_2O_3 are expected to provide catalytic sites for H_2 "spillover" [15-17]. After testing at 550°C for hundreds of hours, all particles in Fe_2O_3/ZrO_2 without IrO_2 grew from 50 to 200 nm as expected, see Figure 3d. Similarly, Figure 3e shows that the IrO_2-added Fe_2O_3/ZrO_2 exhibits similar morphologies, but the HRTEM image of Figure 3f suggests that Ir particles (IrO_2 becomes Ir during and after testing) remain relatively unchanged, still spreading uniformly over ZrO_2 and Fe particles. The elemental mapping of Figure 3g further confirms that Fe, Zr and Ir dispense

uniformly within the Fe-bed and there is no apparent Fe accumulation/separation on the surface as previously observed after multiple redox cycle at 750°C [18]. The presence of inert ZrO_2 and low operating temperature are clearly the reason for retaining such a chemical homogeneity [19, 20].

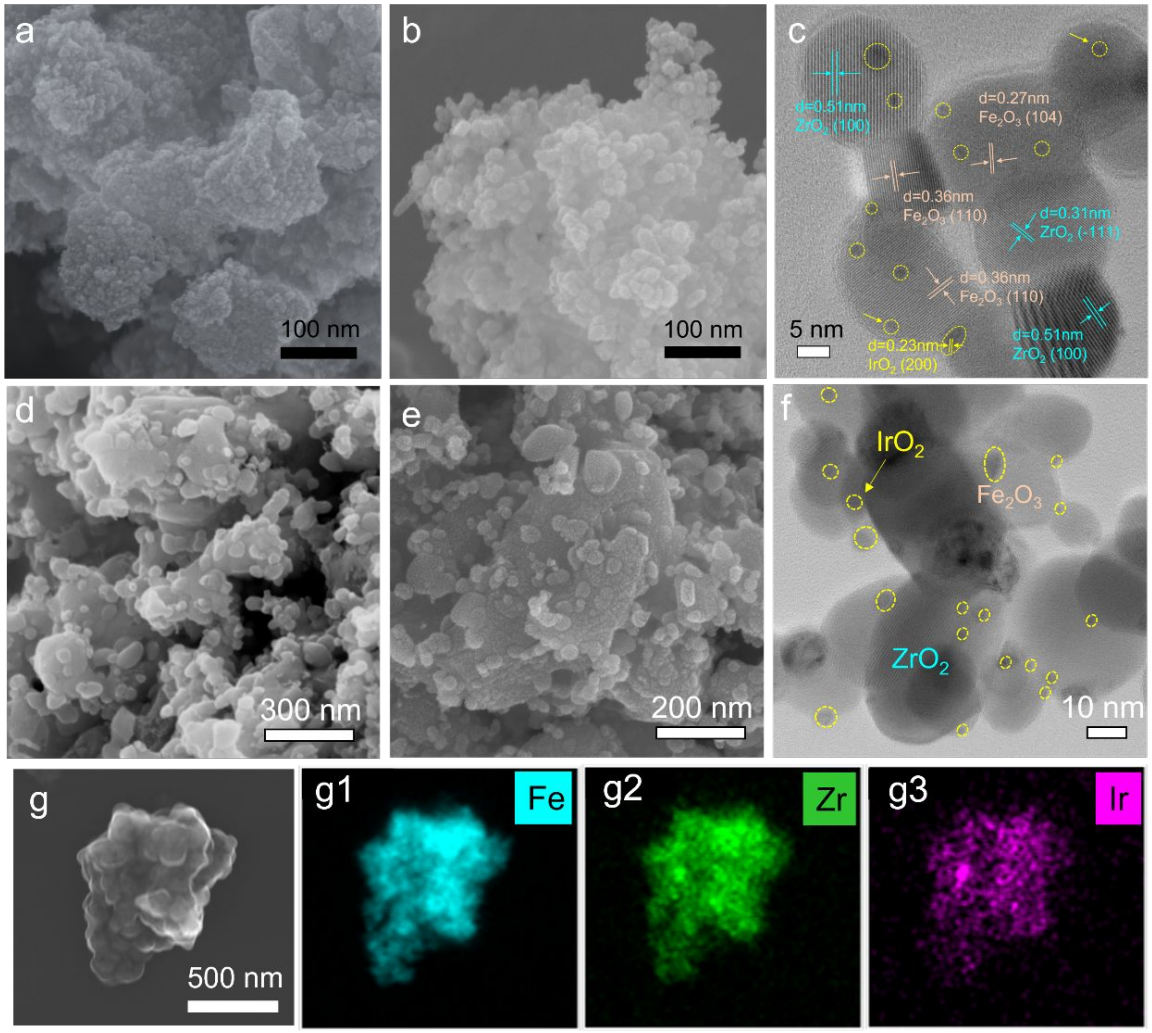

Figure 3. Characterization of the Fe-bed materials: (a) SEM image of fresh Fe_2O_3/ZrO_2; (b) SEM image of fresh Fe_2O_3/ZrO_2-IrO_2; (c) HRTEM image of fresh Fe_2O_3/ZrO_2-IrO_2; (d) SEM image of Fe_3O_4/ZrO_2 after 100h testing; (e) SEM image of Fe_3O_4/ZrO_2-Ir after 100h testing; (f) HRTEM image of Fe_3O_4/ZrO_2-Ir after 100h testing; (g) elemental mapping of Fe_3O_4/ZrO_2-Ir after 100h testing: (g1) Fe, (g2) Zr, (g3) Ir. Note that Fe_2O_3 and IrO_2 turned to Fe_3O_4/Fe and Ir, respectively, after testing.

2.3. Evaluation of electrode overpotential of RSOC

To understand which RSOC component limits the overall performance, we apply the symmetrical three-electrode cell (STEC) method we developed recently to OE [21]. Figure 4a

and 4b show a schematic of the STEC method. The counter electrode (CE) and working electrode (WE) are identical OE of LSM-BYC, while the reference electrode (RE) is a silver wire/Au paste attached to the circumference of the electrolyte disk. Depending on the direction of the DC current applied, EIS spectrum related to either ORR (discharge) or OER (charge) polarization can be obtained. For example, when a positive current density (j) is applied as shown in Figure 4b, obtained EIS spectrum of the OE as an WE is related to the OER process. Figure S9 shows the obtained polarization resistance (R_p) of both ORR and OER *vs.* j at 550-700 ^oC. R_p is observed to decrease with j, which is expected from the *Butler-Vomer* equation. The degree of R_p reduction is more pronounced at lower temperatures, implying the low-temperature dominance of the charge transfer process. At higher temperatures where charge-transfer process is more facile, j has less effect on R_p. It is interesting to mention that OER-R_p of the LSM-BYC becomes noticeably lower than that of ORR at high j, making the polarization curve asymmetrical. This finding is important evidence that LSM-BYC is a better OER electrode than ORR at high j. The R_p stability of the LSM-BYC OE was also evaluated at j = 10 mA cm^{-2} and 550^oC; the results are shown in Figure S10a-S10c. The LSM-BYC electrode shows a good stability for both OER and ORR polarization over ~500 h (it is de facto decreasing with time during the polarization), implying that any performance degradation of RSOC may be related to either HE or electrolyte.

The obtained $R_p(j)$-j data in Figure S9 is further integrated to produce overpotential $\eta(j)$ by

$$\eta(j) = \int_0^j R_p dj \quad (1)$$

The overpotential (η) derived from R_p *vs.* j is shown in Figure 4c. A typical Tafel curve in both OER and ORR domains are clearly observed. We further apply the below *Butler-Volmer* equation (assuming that ORR and OER are multi-step charge transfer processes, but the rate-limiting step involves single electron transfer) to fit the data with exchange current density j_0 and transfer coefficient α as variables [22]:

$$j = j_o\left(exp\left(\frac{-\alpha F\eta}{RT}\right) - exp\left(\frac{(1-\alpha)F\eta}{RT}\right)\right) \quad (2)$$

where F, R and T have their usual meanings. The results are shown in Figure 4d and 4e as a function of temperature. Clearly, j_o follows Arrhenius relationship with an activation energy E_a=1.38 eV, while α is insensitive to T and averaged to be ~ 0.38 over 550-700°C.

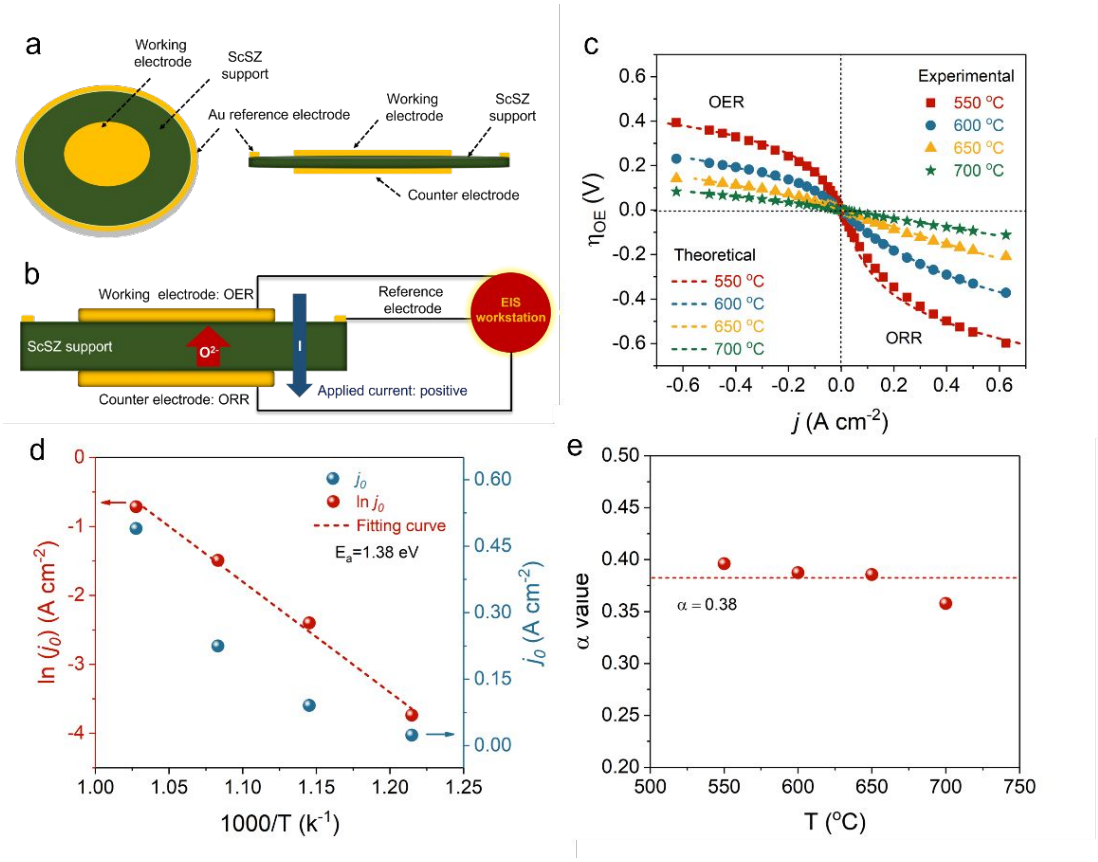

Figure 4. (a) and (b) Schematic of STEC method; (c) η_{OE} *vs.* j; (d) ln (j_0) *vs.* 1/T and α *vs.* T.

With η_{OE} in Figure 4c and combining the overall V-j curve from the full cell, the anode overpotential η_{HE} can be separated by the following equations

$$\eta_t = \pm (E_N - V_C) \quad (3)$$

$$\eta_{HE} = \eta_t - (\eta_{ohm} + \eta_{OE}) \quad (4)$$

where η_t is the total overpotential; "+" for ORR and "-" for OER; $\eta_{ohm} = jR_o$, where R_o is ohmic resistance obtained from EIS; V_C and E_N are cell voltage of the full cell and Nernst potential, respectively.

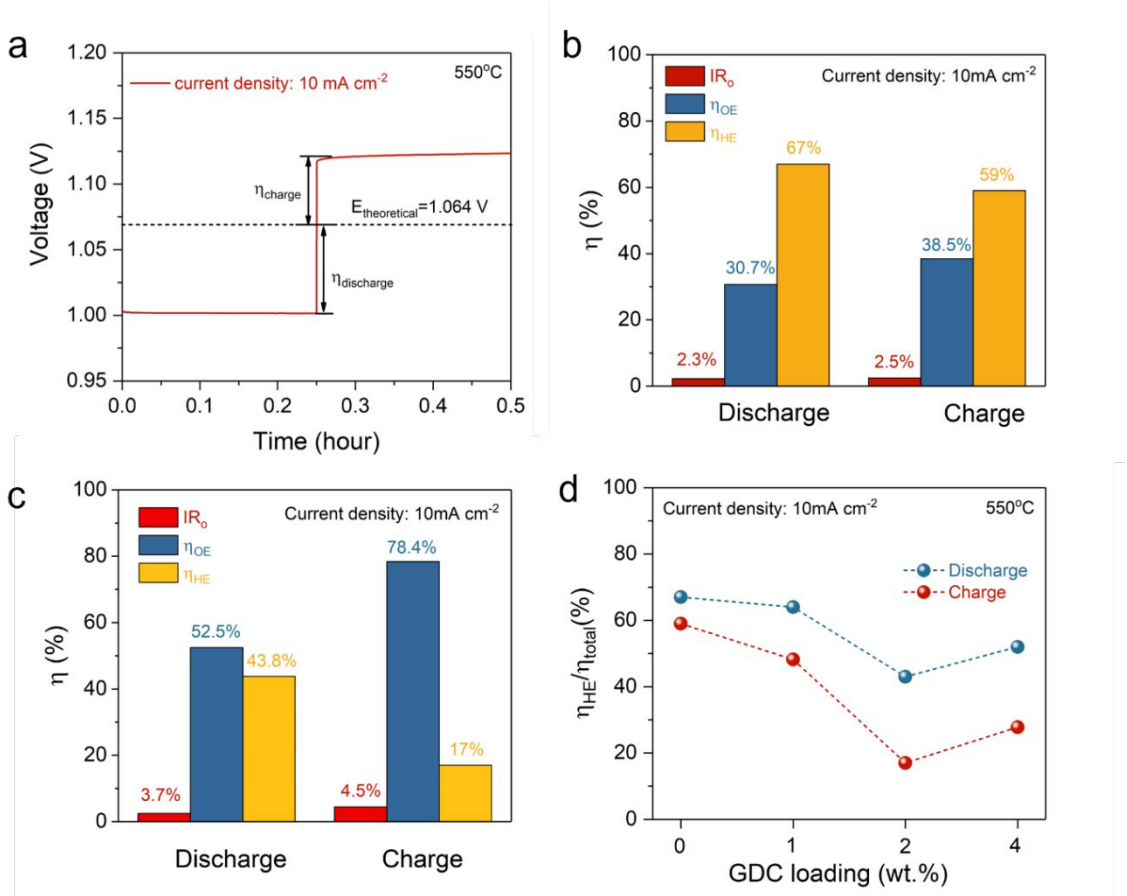

Figure 5. (a) A typical discharge and charge profile of SOIAB at j= 10mA cm^{-2} with U_{Fe}=5% of a baseline cell; (b) η distribution among different cell components of the baseline cell; (c) η distribution among different cell components of the 2 wt.% GDC-modified cell; (d) η contribution from HE for different GDC loadings.

Figure 5a shows a typical discharge and charge profile of the battery at j=10 mA cm^{-2} (0.2 C) and U_{Fe}=5%. Based on the profile and eq. (3), η_t of discharge and charge processes is obtained

separately. The results in Figure 5a suggest a slightly higher η_t for discharge than charge, which is consistent with the observation of higher R_p for ORR (discharge) than OER (charge) shown in Figure S9. After separating η contributions from cell components, Figure 5b and 5c compare them among cell components for the baseline cell and GDC-modified cell. Without GDC in HE, η_{HE}, accounts for 67% and 59% for discharge and charge, respectively. In contrast, the percentages drop to 43.8 and 17% for 2 wt.% GDC-added HE. This comparison illustrates the dominance of HE in the overall performance of the baseline battery. Figure 5d plots the effect of GDC loading on η_{HE}, suggesting that 2 wt.% is the optimal GDC loading. For η_{HE} with other GDC loadings, refer to Figure S11. The optimal GDC loading at 2 wt.% is understood to be the result of balanced reactive sites between GDC and Ni phase. In other words, too much GDC may cover and block more active Ni particles for the reactions. The improved RSOC performance is also illustrated in Figure S12 and S13.

2.4 Electrochemical performance evaluation of SOIAB

Figure 6a shows the voltage profiles vs. time during cycle at different C rates varying from 0.1 C (5 mA cm^{-2}) to 1.5 C (75 mA cm^{-2}) but a fixed U_{Fe}= 10% for both baseline and IrO_2-added batteries (containing 0.001 mol active Fe); the corresponding RTE calculated is shown in Figure 6b. As expected, the battery's RTE decreases with C-rate, varying from 96% at 0.1 C to 63.9 % at 1.5 C for the IrO_2-battery. In contrast, the baseline battery already exhibits a lower RTE=58% at 0.6 C (j=25 mA cm^{-2}). The introduction of IrO_2 clearly improves the C-rate performance, particularly during the charging cycle by boosting the FeO_x-reduction kinetics. When the C-rate returns to 0.1 C, a high RTE=95.2% is still achievable.

The U_{Fe} influences SOIAB's RTE and energy density. Figure 6c shows voltage profiles at different U_{Fe} under a fixed j=10 mA cm^{-2} (0.2 C). As U_{Fe} is increased from 5 to 100%, the total discharge time is increased proportionally from 15 to 300 min; see SI for the calculation. In this study, only one cycle at each U_{Fe} was performed to show the effect of U_{Fe} on specific energy density. The low and high cutoff voltages were set to 0.6 and 2.0 V for discharge and charge cycle, respectively. From the results shown in Figure 6c, it is evident that the IrO_2-battery can be cycled with a stable voltage plateau even at U_{Fe}=100%. However, the discharge voltage of the baseline battery experiences a sharp decrease and reaches the cutoff voltage quickly after U_{Fe}>80%, implying a severe mass transport limitation, likely caused by the depletion of Fe due to the insufficient reduction of FeO_x during the charging cycle.

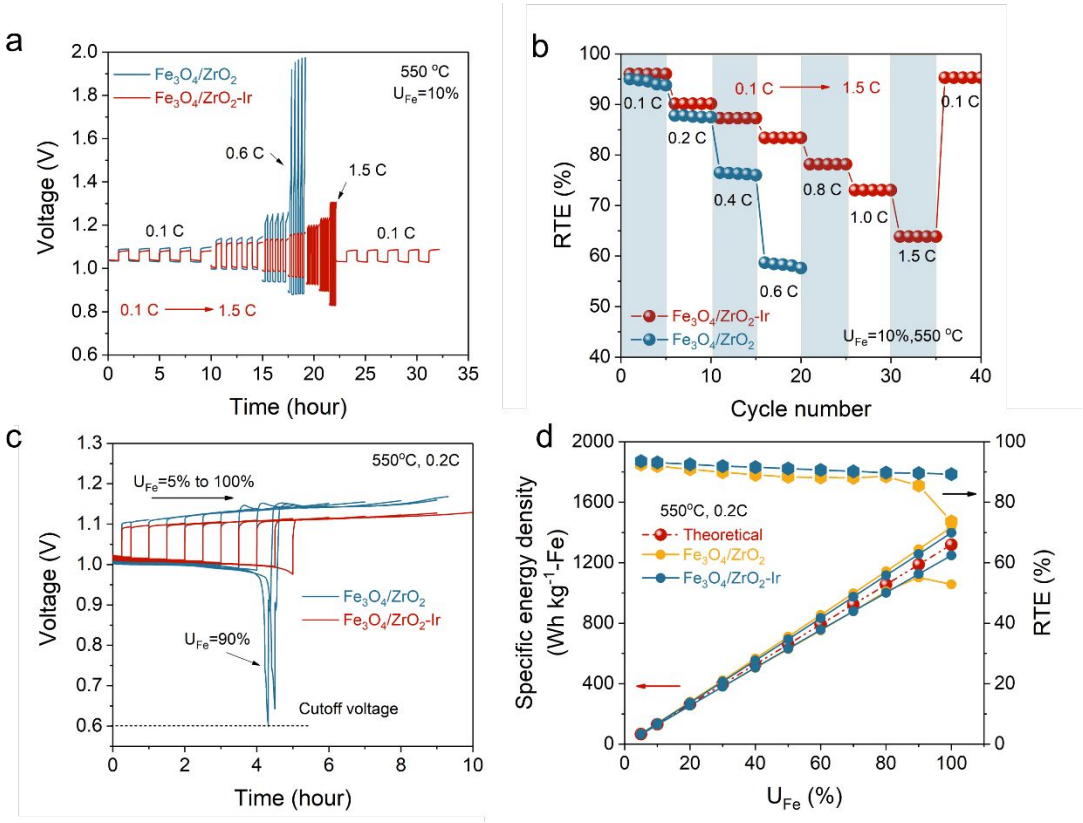

Figure 6. Electrochemical performance of baseline and IrO_2-battery. (a) Voltage profile *vs.* time during cycle at different C rates; (b) effect of C-rate on RTE; (c) voltage profiles vs. time at a fixed j= 10 mA cm^{-2} (0.2 C) and different U_{Fe} (5-100%); (d) discharge and charge SED and corresponding RTE *vs.* U_{Fe}.

The discharge and charge specific energy density (SED) and RTE are further calculated from Figure 6c and plotted in Figure 6d as a function of U_{Fe}. With an increase of U_{Fe}, both discharge and charge SED (based on Fe mass in the Fe-bed) increase, achieving discharge SED (DSED) of 63.8, 254, 631 and 1,248 Wh kg^{-1}-Fe at U_{Fe} of 5, 20, 50 and 100%, respectively. The deviation between the theoretical and experimental values increases with U_{Fe}, which reflects the mass transport limitation. It is also noted that RTE is only deceased by ~5% (from 93.6 to 89.3%) as U_{Fe} is increased from 5 to 100%. Overall, the introduction of IrO_2 into Fe_2O_3/ZrO_2 has not only significantly improved the C-rate performance, but also enabled the battery to operate at higher U_{Fe}.

2.5 Long-term stability at different U_{Fe} of SOIAB

The long-term stability of the baseline and IrO_2-SOIAB at 0.2C (j=10 mA cm^{-2}) and U_{Fe}=5% was first tested and the results are compared in Figure 7a. The IrO_2-SOIAB exhibit a slightly lower charging voltage and marginally better stability than the baseline battery under low U_{Fe} and C-rate condition. The corresponding discharge and charge SEDs, (DSED and CSED, respectively) of the IrO_2-battery are shown in Figure 7b, indicating DSED=63.2 Wh kg^{-1}-Fe, CSED=69.2 Wh kg^{-1}-Fe and RTE=91.3% at U_{Fe}=5% after 500 cycles (0.25h per cycle duration). Figure S14 shows the baseline SOIAB with similar performance, *e.g.,* DSED=62.0 Wh kg^{-1}-Fe, CSED=69.0 Wh kg^{-1}-Fe, and RTE=90% after 250 cycles. While under low U_{Fe}, both baseline and IrO_2 batteries show a similar long-term performance, their stability and RTE at a high U_{Fe} are more meaningful for practical applications since LDES requires large energy capacity, which can be achieved by operating at high U_{Fe}.

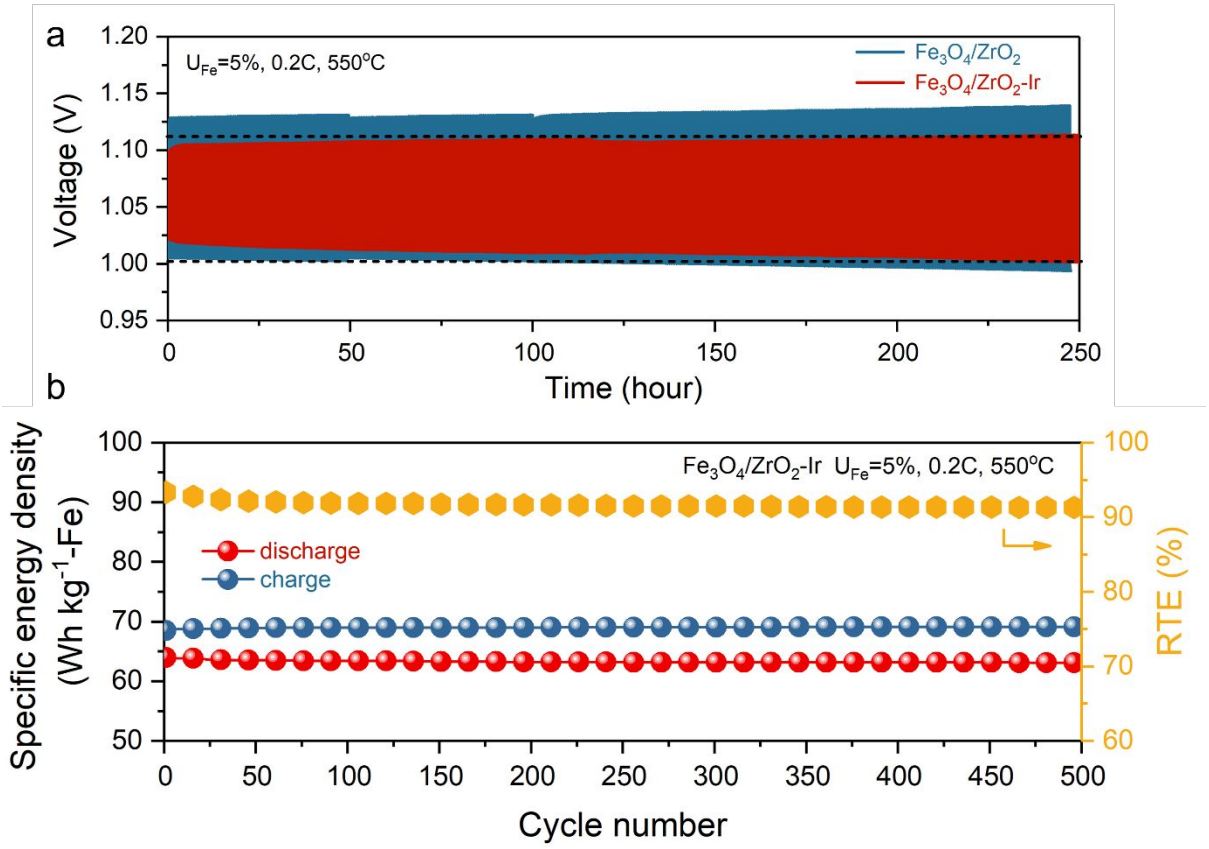

Figure 7. (a) Comparison of cycle stability of SOIAB with different ESU materials; (b) the corresponding SED and RTE of SOIAB with Fe_3O_4/ZrO_2-Ir ESU materials operated at U_{Fe}=5% and 0.2C.

We, therefore, performed a comparative long-term test on both baseline and IrO_2-batteies at U_{Fe}=50% and 0.2C (j=10 mA cm^{-2}). Figure 8a compares cyclic voltage profiles of the two cells. The baseline cell clearly exhibits a pronounced degradation under this condition, failed at charging where the voltage hit 2.0V (the high cutoff voltage) after 80 hours. This is likely because the kinetic rate of Fe-oxide reduction (charging process) is insufficient to match up the charging current density due to the thicker FeO_x layer formed under high U_{Fe}. In contrast, the cyclic voltage is much more stable for the IrO_2-battery. Interestingly, the cell eventually hit 0.8 V (the low cutoff voltage) during discharge after 200 hours. The fact that the IrO_2-cell exhibits stable charging voltage and declining discharging voltage during 200-hour cycling implies that the oxidation of Fe becomes rate limited, which is understandable given that the FeO_x reduction

kinetics has been effectively boosted by IrO_2 catalyst. Within the stable performance of 200 hours (or 40 cycles of 2.5 hour/cycle), the IrO_2-battery exhibits a DSED of 617.6 Wh kg^{-1}-Fe at RTE=87.4% under U_{Fe}=50% and j=10mA/cm^2 (0.2C), much better than the baseline cell (see Figure 8b). Overall, compared to the previously published results, the IrO_2-battery represents a significant improvement in capacity, RTE and cycle stability [9-11, 13, 23, 24]. Therefore, using a small amount of expensive IrO_2 in Fe-bed is justified for SOIAB. To increase the cycle duration for practical LDES application, the mass of Fe-bed needs to be increased accordingly as shown in Figure S1b. Obviously, greater amount of Fe-bed requires a larger anode chamber, which ultimately increases the size of ROSC and the magnitude of charge/discharge current densities.

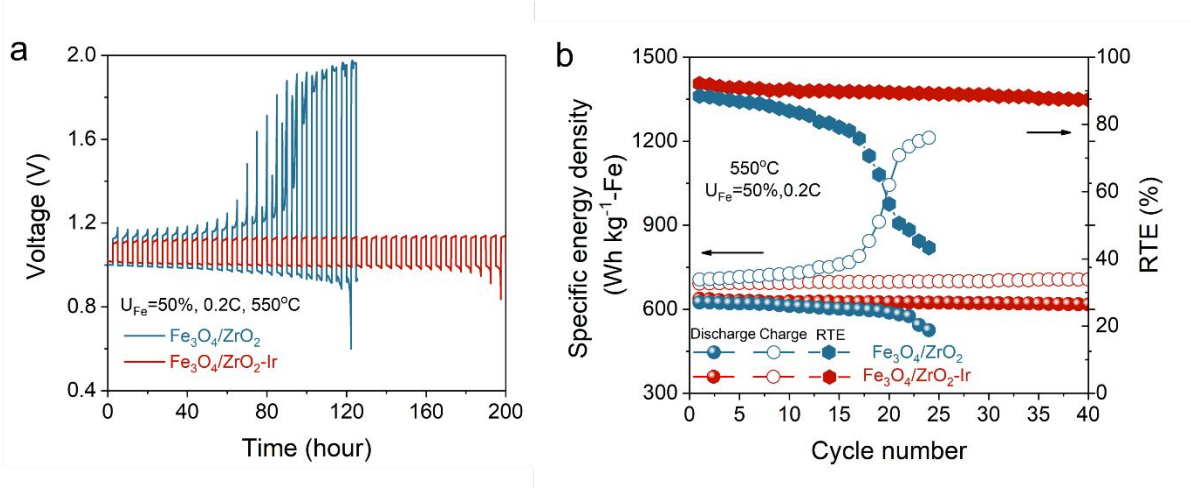

Figure 8. Battery performance tested at U_{Fe}=50% and 0.2C for different ESU materials: (a) voltage profiles; (b) SED and RTE vs. cycle number.

To truly demonstrate SOIAB's LDES capability, we further assembled an SOIAB with more Fe-mass (in this case 0.28g or 0.005 mol) in the Fe-bed. This is the maximal amount of Fe we can pack within ϕ1″ cell without H_2/H_2O gas transport limitation. This amount of Fe-mass enables a cycle duration of 12.5 h at 10 mA cm^{-2} and U_{Fe}= 50%. The measured voltage profiles are shown in Figure 9a. Translating Figure 9a into battery performance, Figure 9b shows that

an RTE ~90% has been achieved with a high DSED= 625 Wh/kg-Fe. This level of performance demonstrates a great potential of SOIAB for LDES applications, even with a lab-size SOIAB. More important to practical applications, a simple multiplication (n) of Fe-mass used in this work will result in a cycle duration of greater than 12.5 hours as the size of SOIAB is increased correspondingly.

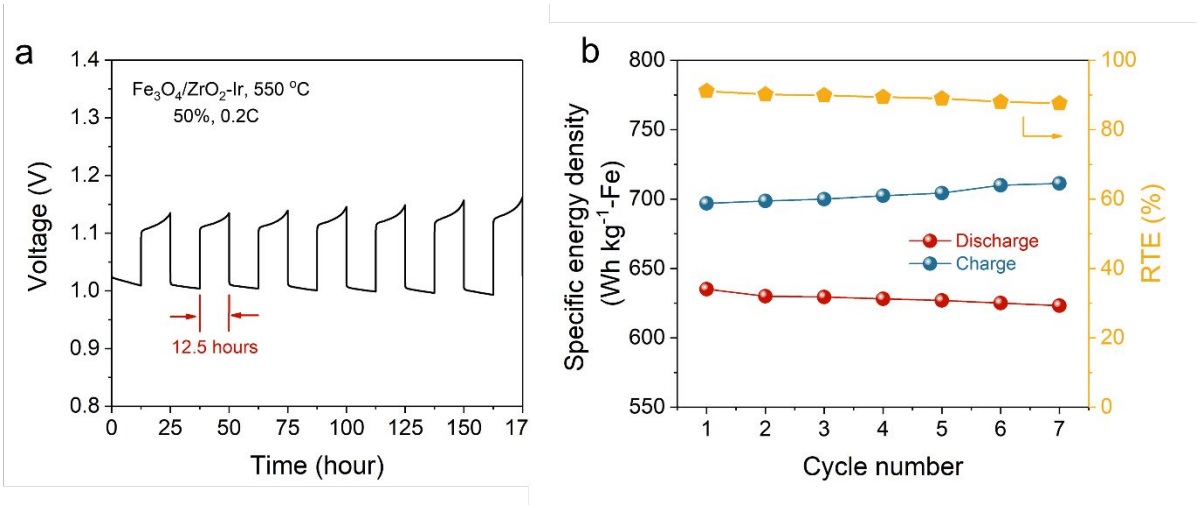

Figure 9 The charge-discharge performance of SOIAB (a single cell with 0.28g active Fe mass, enabling 12.5 h cycle duration at 10 mA cm^{-2} and U_{Fe}=50%): (a) voltage profiles; (b) corresponded SED and RTE vs. cycle number.

Despite the promising LDES performance, SOIABs still face engineering challenges in demonstrating commercially meaningful durability and self-discharge rate, both of which are closely tied to the current development of solid oxide cells (SOCs) for power and hydrogen productions. For example, the self-discharge rate of SOIABs is determined by the gas tightness of SOCs, which is also a high standard for SOC operations. The same argument can be applied to the durability concern. Therefore, as SOCs engineering advances toward commercialization, so will SOIABs.

2.6 Understanding the mechanism of IrO_2-catalyzed Fe-oxide reduction kinetics

IrO_2 has been known as an excellent catalyst for many chemical reactions [25-27]. In the context

of H_2 reduction, IrO_2 will be reduced to Ir, which acts as catalytic to H_2 spillover. To better understand the fundamental catalysis effect of introducing Ir, density functional theory (DFT) calculations were performed to elucidate how Ir catalyzes H_2 reduction of Fe_3O_4 process. Details on the calculation method and structure of Fe_3O_4 can be found in the Experimental section and Figure S15.

Figure 10a shows that, on the pure Fe_3O_4 surface, the relative energy for H_2 dissociative adsorption (or spillover) on the Fe_3O_4 (111) surface (H_2-ads) is -4.62 eV. After dissociation, one H atom needs to overcome 0.78 eV energy barrier (-4.62 eV vs. -3.84 eV) to migrate to the adjacent O atom on the surface, while another H bonds with the adjacent Fe atom, to reach the first transition state 1 (TS1). However, a further breaking Fe-H bond to allow H atom to migrate toward O atom for H_2O formation requires a much higher 1.16 eV energy barrier (-4.46 eV vs.-3.48 eV), to reach transition state 2 (TS2).

In the Fe_3O_4-Ir case, however, two Fe-O bonds are found broken, leading to O protrusion out of the surface and formation of a new elongated Fe-O bond, see Figure 10b and Figure S16. Comparatively, the energy for H_2 spillover on the surface of Ir atom (H_2-dis) are lower (-4.93 eV) than pure Fe_3O_4-case (-4.62 eV), suggesting the catalytic effect of Ir on H_2 spillover. While the energy level to reach TS1 are not significantly different for both cases, there is a considerable difference in the FS1 state. For the Fe_3O_4-Ir case, the final FS1 energy is -6.08 eV, decreased from -4.15 eV at TS1, while there is only a slight decrease from -3.84 (TS1) eV to -4.64 eV (FS1) for the pure Fe_3O_4 case.

The final step of the H-migration, from FS1 to FS2, with two H atoms separately adsorbed to O atom of the Fe_3O_4-Ir surface, which is equivalent to 0.40 eV energy barrier (-6.08 eV vs. -

5.68 eV), significantly lower than that of pure Fe_3O_4 case (1.16 eV). Therefore, it is concluded that the presence of Ir can greatly promote H-migration and breaking of Fe-O bonds, leading to a boosted reduction kinetics of Fe_3O_4.

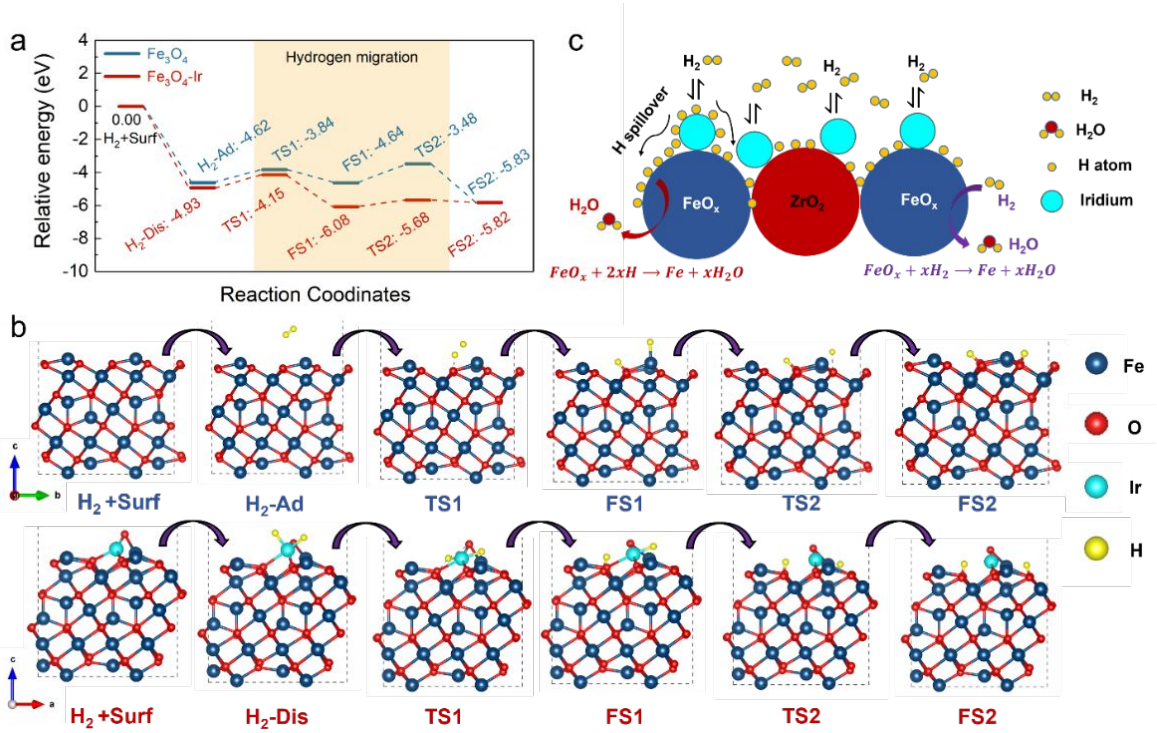

Figure 10. (a) Calculated energetics of initial, transition (TS) and final states (FS) for H_2 dissociative adsorption and migration on Fe_3O_4 (111) and Fe_3O_4-Ir (111) surface. (b) The optimized H_2 dissociative adsorption and migration structures at Fe_3O_4 (111) surface with/out Ir. (c) A schematic representation of pathways in Fe_3O_4/ZrO_2-Ir reduction process.

Corresponding to the DFT model, we also sketch Figure 10c to illustrate physically the pathways of FeO_x reduction process in the presence of Ir catalyst, which includes surface H_2 spillover on Ir and migration of the activated H atoms from an Ir nanoparticle onto FeO_x lattice.

The lowered activation energy of Fe-oxide reduction by Ir is indeed experimentally observed by Temperature Programmed Reduction (TPR). Figure 11a shows the TPR profiles of the baseline and Ir-added samples. The baseline sample exhibits three reduction peaks located at 297.2, 416 and 641.4 ^oC, which can be assigned to the reduction of Fe_2O_3-to-Fe_3O_4, Fe_3O_4-to-FeO and FeO-to-Fe, respectively. After adding Ir into Fe_2O_3/ZrO_2, only one Fe-oxide reduction

peak is observed at 461.1 °C, signaling a significantly improved reaction kinetics.

To quantify the reduction kinetics, we applied Kissinger's method [28] to extract the activation energy of the reduction process. From the peak temperature, T_{max}, of a TPR profile, the following relationship holds:

$$\ln\left(\frac{\Phi}{{T_{max}}^2}\right) = -\frac{E_a}{RT_{max}} + \ln\left(\frac{AR}{E}\right) + C \quad (5)$$

where Φ is the ramping rate; E_a is the activation energy of reduction process; C is a constant; A is the pre-exponential term; R is the universal gas constant. Since E_a is a constant for a fixed thermal process, by plotting $\ln\left(\frac{\Phi}{{T_{max}}^2}\right)$ vs. $\frac{1}{T_{max}}$, the slope ($-E_a/R$) can be obtained from the Arrhenius plot.

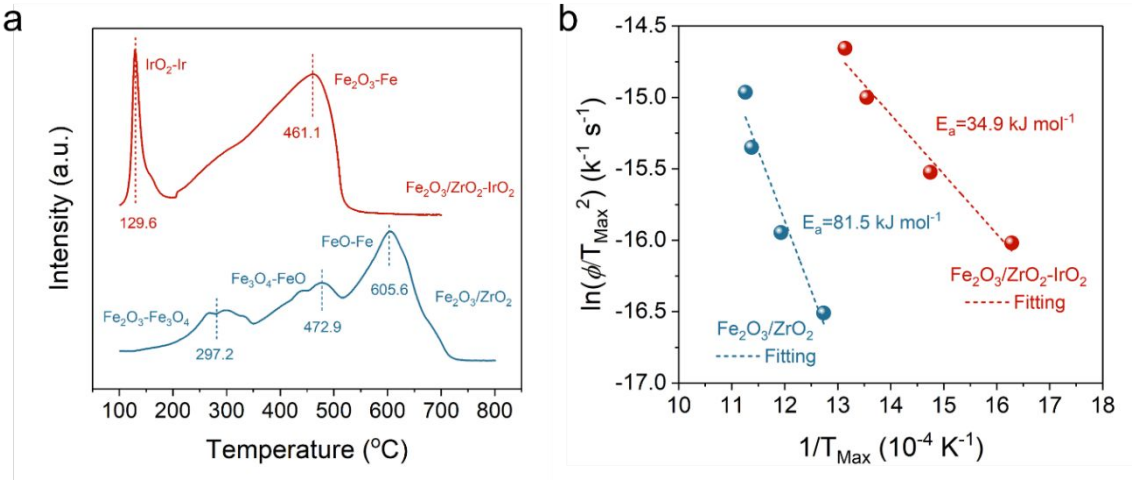

Figure 11. (a) TPR profiles of baseline and IrO_2-added samples at a ramping rate of 10 °C/min; (b) Arrhenius plots of $\frac{\Phi}{{T_{max}}^2}$.

Figure 11b shows the Arrhenius plots of the two samples, from which the activation energy E_a for the baseline and Ir-added samples are calculated as 81.5 and 34.9 kJ mol^{-1}, respectively, suggesting that IrO_2 significantly lowers the energy barrier for FeO_x-reduction kinetics. Figure S17 shows the original TPR profiles at different ramping rates from 2.5 to 15 °C/min.

3. Conclusion

In summary, this study has demonstrated SOIAB with significantly improved energy storage performance at long cycle duration, moving this new battery technology a step closer to practical LDES applications. The storage performance improvement was realized through optimizations in electrolyte, electrodes, and energy storage materials. The use of three electrode configuration allows us to pinpoint the overpotential contribution from OE, through which the overpotential contributions from other cell components are deconvoluted as a function of current density after combining with the cell voltage, ohmic resistance and Nernst potential of a full battery. The finding is that HE contributes a majority of overpotential to the total cell voltage loss. Adding GDC catalyst into HE substrate appreciably lowers the overpotential of HE, thus improving battery cell performance. In the meanwhile, after introducing Ir nanoparticles into Fe-based ESU, the slow Fe_3O_4 reduction kinetics related to the charging process has been significantly boosted. We show computationally that Ir can drastically lower energy barriers for H_2 spillover and breaking of Fe-O bond, thus promoting the Fe_3O_4 reduction kinetics. With all the improvements made in battery materials, we finally demonstrate multiple 12.5-h cycles with high DSED (625 Wh/kg-Fe) and RTE (87%). Overall, given the excellent low C-rate performance and low-cost Fe, it is reasonable to consider SOIAB as a LDES-compatible device. With the scaled-up SOIAB systems, achieving electricity storage with 10+ hour, daily, weekly, monthly and even seasonal cycle is expected.

4. Experimental Section

4.1. Synthesis of materials

4.1.1 Fe-bed ESU materials

The starting baseline Fe-bed (the energy storage material) is a mixture of Fe_2O_3 and ZrO_2.

During operation in SOIAB, Fe_2O_3 is first reduced to metallic Fe, on which Fe/Fe_3O_4 becomes the active redox couple to regular oxygen transported through RSOC during charge/discharge cycles. The fresh baseline Fe_2O_3/ZrO_2 mixture was prepared by a co-precipitation method. Briefly, the stoichiometric solutions of $Fe(NO)_3•9H_2O$ (⩾ 99.999%, Sigma-Aldrich) and $ZrO(NO)_2•xH_2O$ (⩾99.999%, Alfa-Aesar) in a molar ratio of Fe:Zr=85:15 were first dissolved in deionized water separately. Then the two solutions were mixed in a beaker with a cation concentration of 0.1 M. The resultant clear orange solution was then added dropwise to an $(NH_4)_2CO_3$ (Sigma-Aldrich) solution bath under a constant stirring. To ensure a full precipitation of all cations in the solution, the molar ratio of $(NH_4)_2CO_3$ and M^{n+} (M= Zr and Fe) was kept as $n(NH_4)_2CO_3:nM^{n+}$=2.0:1. The resultant brownish precipitate was then left in the solution for 20 h with continuous stirring. Finally, the aged suspension was filtered and washed several times with ethanol, dried overnight at 80 ^oC and calcined in air at 600 ^oC for 5h to yield the Fe_2O_3/ZrO_2 product.

To obtain the IrO_2 impregnated Fe_2O_3/ZrO_2, the as-prepared Fe_2O_3/ZrO_2 was first ball milled using a planetary ball mill (BM4X-04, COL-INT TECH) in a zirconium container for 20 h with a milling speed of 300 rpm. Then, 0.1 g Ir precursor, iridium III 2,4-pentanedionate ($C_{15}H_{21}IrO_6$, Sigma-Aldrich) dissolved in 2mL acetone (99.5%, Sigma-Aldrich) was added into 1 g of milled Fe_2O_3/ZrO_2 powders in an agata mortar followed by mixing and grinding. Finally, the impregnated powders were calcined at 600^oC for 2h. The total IrO_2 loading in the ESU is around 4 wt.% of Fe_2O_3/ZrO_2 mass. During operation, IrO_2 turns into metallic Ir as a catalyst in the Fe-bed of the battery.

4.1.2 $La_{0.8}Sr_{0.2}MnO_3$ (LSM)/$(Bi_{0.75}Y_{0.25})_{0.93}Ce_{0.07}O_{1.5}$ (BYC) OE

The LSM/BYC composite OE was prepared by combustion method using nitrates as the metal precursors. Briefly, for LSM preparation, stoichiometric amounts of $La(NO_3)_3 \cdot 6H_2O$ (Sigma-Aldrich), $Sr(NO_3)_2$ (Sigma-Aldrich) and $Mn(NO_3)_2 \cdot 4H_2O$ (Sigma-Aldrich) were dissolved into 500 mL 0.2 M citric acid (CA, Sigma-Aldrich) solution with a molar ratio of metal ions:CA=1:2. Then 10 mL nitric acid (70%, Sigma-Aldrich) solution was added into the mixture solution under stirring. The pH of the solution was then adjusted to ~ 6 with ammonia (28%-30%, Sigma-Aldrich). Finally, the transparent solution was heated in an oven at 240 ^oC until auto-combustion. The obtained powders were then broken up and calcinated at 900 ^oC for 5h. The BYC powders were prepared by a similar process with $Bi(NO_3)_3 \cdot 5H_2O$ (Sigma-Aldrich), $Y(NO_3)_3 \cdot 6H_2O$ (Sigma-Aldrich), and $Ce(NO_3)3 \cdot 6H_2O$ (Sigma-Aldrich) as the metal precursors, except the molar ratio of the metal ions to CA is 1:1.5 and the calcination temperature is 700 ^oC.

4.2. Fabrication of HE-supported electrolyte

The HE-substrate was firstly prepared by dry-pressing method. Briefly, NiO, ScSZ and carbon powders with a weight ratio of 6:4:3 were ball-milled for 4 hours in ethanol with ZrO_2 balls. Then the slurry was dried overnight at 80 ^oC. The dried powders were then fully mixed with 5 wt.% PVB in acetone with an agate mortar, followed by pressing into pellets of $\phi 1.0''$ and partially sintering at 900 ^oC for 2h to achieve enough strength. The HE functional layer was deposited by dipping the HE pellet into a slurry containing NiO:ScSZ=60:40 (wt.%) mixture with a 10 wt.% carbon for 15 s. Then the pellet was pull out of the suspension and dried in an oven for 10 min. The pellet was subsequently sintered at 800 ^oC for 2h, after which a thin layer of ScSZ electrolyte was deposited on top of the functional layer by the same dip-coating

technique. The recipe of the electrolyte slurry is like the functional layer but without NiO. The HE, functional layer and electrolyte triple-layers were finally co-sintered at 1350 ^{o}C for 5h. The final product was ground down to ~400 μm thickness. The thicknesses of the ScSZ electrolyte and HE functional layer are both ~10 μm with a diameter of 0.8 inch.

4.3. Infiltrating GDC nanoparticles into HE substrate

$Gd_{0.2}Ce_{0.8}O_2$ (GDC) nanoparticles were infiltrated into the NiO-ScSZ HE substrate to improve the HE performance. To do so, 0.5 M nitrate solutions of GDC precursors were prepared by dissolving stoichiometric amount of $Gd(NO_3)_3 \cdot 6H_2O$ (Sigma-Aldrich) and $Ce(NO_3)_3 \cdot 6H_2O$ (Sigma-Aldrich) in a distilled water with 20 vol.% ethanol. Ethylene diamine tetraacetic acid (EDTA, Sigma-Aldrich) and citric acid (CA, Sigma-Aldrich) as a surfactant and chelating agent, respectively, dissolved into a diluted ammonia was then added into the GDC precursor solution. The pH of the solution was carefully adjusted to 8. The molar ratio of CA to EDTA to metal ions was kept at 2:1:1. Figure S18 shows process of the HE infiltration along with half-cell fabrication steps. After infiltration, the NiO-ScSZ/ScSZ half-cell was fired in air at 500 ^{o}C for 1h to decompose metal nitrates into their respective oxides. The loading of GDC was controlled by the number of infiltration and determined based on the mass change before and after infiltration.

4.4. Single cell fabrication

Two types of cells were fabricated in this work to examine the battery performance: (i) HE-supported full cell and (ii) electrolyte-supported symmetrical cell. For the HE-supported full cell, OE was made by screen printing the OE ink on top of the ScSZ electrolyte surface. The ink consists of a mixture of LSM, BYC and a V-006 binder (Columbia International) in a

weight ratio of LSM:BYC:V-006 = 40:60:150. After printing and drying, the cell is calcined at 800 ^{o}C for 2h to make the final cell. The effective surface area of the cathode electrode is 1.4 cm^2, and the silver mesh and gold paste were used as current collectors for both OE and HE.

For the electrolyte-supported symmetrical three-electrode cell, the ScSZ electrolyte with a thickness of 200 μm was made by tape casting method. The same cathode as the full cell was screen-printed symmetrically on both sides of the ScSZ electrolyte and then fired at 800 ^{o}C for 2 hours. To make the third reference electrode, a silver wire was wound and fixed by gold paste along the circumference of the electrolyte pellet, see Figure S19.

4.5. Battery cell assembly and testing

For a typical battery testing, the ESU material (0.056 and 0.28g Fe for short and long-duration cycles) was first sped over an Al_2O_3 wool and then loaded into the chamber of battery holder layer by layer to ensure minimal mass transport limitation. Then, the RSOC was placed into the grove of the holder with the HE substrate facing down. A layer of glass slurry consisted of glass powder (from Schott GM31107) mixed with binder was then applied along the perimeter between the cell and holder. The current collection wires on the HE-side were carefully routed through an insulating glass ring and the glass layer to avoid short circuiting with the metal holder.

The electrochemical performance of the battery was tested using a Solartron Multichannel system (model 1470e) in conjunction with a Solartron 1255 frequency response analyzer. The battery was first heated in the air from room temperature to 680 ^{o}C and held for 30 min to melt the glass and achieve gas tightness. Then, the temperature was decreased to 550 ^{o}C for testing. A 5% H_2/N_2 at 50 cm^3/min was first introduced into the HE-chamber for 50 minutes to purge

the residual air, then switched to pure H_2 through a room temperature water bubbler to reduce the HE and Fe-bed into their metallic states. The open-circuit voltage (OCV) of the battery cell was constantly monitored and used to judge the completion of the reduction process. Once it is done, the initial V-*j* curves and EIS of the RSOC were first measured under OCV in flowing 3% H_2O-H_2. Then the H_2 outlet and inlet valves were closed in sequence and the OCV was monitored until it reached the theoretical potential of 1.067 V (for Fe-Fe_3O_4 redox couple at 550 ^oC). Now the battery is ready for discharge/charge cycling. The MultiStat software is used for collecting data and performing data analysis. The rate performance, U_{Fe} and cycle stability were systematically evaluated based on the protocol given in Table S1. The cutoff voltages for discharge and charge are set at 0.8 and 2.0 V, respectively.

4.6. Materials characterization

The phase compositions of the prepared Fe_2O_3/ZrO_2 composite, LSM and BYC were examined by X-ray diffraction operated at a scan rate of 2^o min^{-1} from 10 to 80^o using Rigaku D/MAX-2100. The morphologies of the Fe-bed materials and battery cell components were examined by a field emission scanning electron microscope (FESEM) (Zeiss Gemini500) with Energy Dispersive X-Ray Spectroscopy (EDS) for elemental mapping analysis. A high-resolution transmission electron microscope (HRTEM, HITACHI H-9500) and scanning transmission electron microscope (STEM, HITACHI SU9000) was also used to examine the infiltrated GDC nanoparticles. The focused-ion-beam technique (FIB, Hitachi NB-5000) was used to prepare TEM samples.

4.7 Computational details

All the calculations were performed using the Vienna Ab Initio Simulation Package (VASP)

based on the density functional theory (DFT) [29, 30]. The projector augmented wave approach [31, 32] was adopted to describe the interaction of ion and electron, and the general gradient approximation in the Perdew-Burke-Ernzerhofer form was employed for electronic exchange-correlation functional [33]. In the simulations, Fe_3O_4 (111) surfaces with a vacuum width of 22 Å were investigated based on the previous report that shows (111) as the most stable surface [34]. Each (111) surface unit was consisted of 12 single layers with tetrahedral Fe termination, in which the atoms of top 3 layers were relaxed, and others 9 layers were fixed in all surface calculations. The spin polarization was considered in all calculations. The cutoff energy for the plane wave basis expansion was set to 500 eV. The structure optimization was obtained until the force on each ion dropped below 0.05 eV/Å, and the energy was smaller than 10^{-4} eV. In this work, the Monkhorst-Pack scheme k-points sampling [35] was used for integration in the first Brillouin zone, and the separation of the k-point mesh was < 0.03 $Å^{-1}$. The migration energy barrier of H on different surfaces was calculated by locating the transition states, which can be obtained by analyzing the minimum-energy path for the H-diffusion processes using the climbing-image nudged elastic band method. In addition, Van Der Waals correction was carried out for the interactions between the adsorbed H_2 molecule and the surface. For an accurate treatment of the electron correlation in the localized 3*d*-Fe orbital, we have used rotationally invariant density functional theory, and an effective U_{eff} = 3.8 eV was used to calculate the on-site Coulomb interaction of Fe-3d states [36].

Acknowledgement

We would like to thank National Science Foundation for the financial support under award number 1801284 and Department of Energy, Office Fossil Fuels, National Energy technology

Laboratory for the financial support under award number DE-FE-0032111, Natural Science Foundation of China (Grant No. 12164020). We also gratefully acknowledge Hefei Advanced Computing Center for computational times.

References

1. P. Denholm and M. Hand, *Energy Policy*, 2011, **39**, 1817-1830.
2. W. A. Braff, J. M. Mueller and J. E. Trancik, *Nature Climate Change*, 2016, **6**, 964-969.
3. M. R. Shaner, S. J. Davis, N. S. Lewis and K. Caldeira, *Energy & Environmental Science*, 2018, **11**, 914-925.
4. O. J. Guerra, J. Zhang, J. Eichman, P. Denholm, J. Kurtz and B.-M. Hodge, *Energy & Environmental Science*, 2020, **13**, 1909-1922.
5. J. A. Dowling, K. Z. Rinaldi, T. H. Ruggles, S. J. Davis, M. Yuan, F. Tong, N. S. Lewis and K. Caldeira, *Joule*, 2020, **4**, 1907-1928.
6. C. A. Hunter, M. M. Penev, E. P. Reznicek, J. Eichman, N. Rustagi and S. F. Baldwin, *Joule*, 2021, **5**, 2077-2101.
7. P. Albertus, J. S. Manser and S. Litzelman, *Joule*, 2020, **4**, 21-32.
8. R. E. Ciez and D. Steingart, *Joule*, 2020, **4**, 597-614.
9. C. Zhang and K. Huang, *ACS Energy Letters*, 2016, **1**, 1206-1211.
10. X. Zhao, X. Li, Y. Gong, N. Xu and K. Huang, *RSC Advances*, 2014, **4**, 22621-22624.
11. X. Zhao, X. Li, Y. Gong and K. Huang, *Chemical Communications*, 2014, **50**, 623-625.
12. X. Zhao, Y. Gong, X. Li, N. Xu and K. Huang, *Journal of The Electrochemical Society*, 2013, **160**, A1241-A1247.

13. C. Zhang and K. Huang, *Chemical Communications*, 2017, **53**, 10564-10567.

14. X. Jin, X. Zhao and K. Huang, *Journal of Power Sources*, 2015, **280**, 195-204.

15. R. Prins, *Chemical Reviews*, 2012, **112**, 2714-2738.

16. W. Karim, C. Spreafico, A. Kleibert, J. Gobrecht, J. VandeVondele, Y. Ekinci and J. A. van Bokhoven, *Nature*, 2017, **541**, 68-71.

17. M. Xiong, Z. Gao and Y. Qin, *ACS Catalysis*, 2021, **11**, 3159-3172.

18. C. Zhang, C. Ji, W. Wang, D. Schmidt, X. Jin, J. P. Lemmon and K. Huang, *Energy & Environmental Science*, 2016, **9**, 3746-3753.

19. Q. Tang, Y. Ma and K. Huang, *ACS Applied Energy Materials*, 2021, **4**, 7091-7100.

20. Q. Tang and K. Huang, *Chemical Engineering Journal*, 2022, **434**, 134771.

21. X. Jin and K. Huang, *Journal of The Electrochemical Society*, 2020, **167**, 124501.

22. L. R. F. Allen J. Bard, *Wiley*, 2001, ISBN: 978-970-471-04372-04370.

23. X. Zhao, Y. Gong, X. Li, N. Xu and K. Huang, *Journal of Materials Chemistry A*, 2013, **1**, 14858-14861.

24. X. Zhao, X. Li, Y. Gong, N. Xu, K. Romito and K. Huang, *Chemical Communications*, 2013, **49**, 5357-5359.

25. S. Cherevko, S. Geiger, O. Kasian, N. Kulyk, J.-P. Grote, A. Savan, B. R. Shrestha, S. Merzlikin, B. Breitbach, A. Ludwig and K. J. J. Mayrhofer, *Catalysis Today*, 2016, **262**, 170-180.

26. F. Shen, Y. Wang, G. Qian, W. Chen, W. Jiang, L. Luo and S. Yin, *Applied Catalysis B: Environmental*, 2020, **278**, 119327.

27. J. Ahmed and Y. Mao, *Electrochimica Acta*, 2016, **212**, 686-693.

28. O. J. Wimmers, P. Arnoldy and J. A. Moulijn, *The Journal of Physical Chemistry*, 1986, **90**, 1331-1337.

29. G. Kresse and J. Hafner, *Physical Review B*, 1993, **47**, 558-561.

30. G. Kresse and J. Furthmüller, *Physical Review B*, 1996, **54**, 11169-11186.

31. G. Kresse and D. Joubert, *Physical Review B*, 1999, **59**, 1758-1775.

32. P. E. Blöchl, *Physical Review B*, 1994, **50**, 17953-17979.

33. J. P. Perdew, K. Burke and M. Ernzerhof, *Physical Review Letters*, 1996, **77**, 3865-3868.

34. G. J. Martin, R. S. Cutting, D. J. Vaughan and M. C. Warren, *American Mineralogist*, 2009, **94**, 1341-1350.

35. H. J. Monkhorst and J. D. Pack, *Physical Review B*, 1976, **13**, 5188-5192.

36. X. Yu, Y. Li, Y.-W. Li, J. Wang and H. Jiao, *The Journal of Physical Chemistry C*, 2013, **117**, 7648-7655.